Planar heterojunction boosts solar-driven photocatalytic performance and stability of halide perovskite solar photocatalyst cell

Chunhua Wang [a], Haowei Huang [b,*], Bo Weng [b], Davy Verhaeghe [b], Masoumeh Keshavarz [a], Handong Jin [a], Biao Liu [d], Haipeng Xie [d], Yang Ding [e], Yujie Gao [b], Haifeng Yuan [a], Julian A. Steele [b], Johan Hofkens [a,c,**], Maarten B.J. Roeffaers [b,*]

[a] Department of Chemistry, KU Leuven, Celestijnenlaan 200F, 3001 Leuven, Belgium
[b] cMACS, Department of Microbial and Molecular Systems, KU Leuven, Celestijnenlaan 200F, 3001 Leuven, Belgium
[c] Max Planck Institute for Polymer Research, Ackermannweg 10, 55128 Mainz, Germany
[d] Hunan Key Laboratory for Super-microstructure and Ultrafast Process, School of Physics and Electronics, Central South University, Changsha 410083, China
[e] Laboratory of Inorganic Materials Chemistry (CMI), University of Namur, 61 rue de Bruxelles, B-5000, Namur, Belgium

ARTICLE INFO

ABSTRACT

The excellent optoelectronic properties of metal halide perovskites (MHPs) have been employed in various photocatalytic applications, but their poor water stability is considered as the main bottleneck for further development. Herein, we protect the light-absorbing $CsPbBr_3$ MHP with a NiO_x and TiO_2 hole and electron extracting layer. This planar $NiO_x/CsPbBr_3/TiO_2$ architecture can easily be fabricated through solution-processing. When applied to selective photocatalytic oxidation of benzyl alcohol, this system presents a 7-fold enhancement of photoactivity and an improved stability for over 90 h compared to $CsPbBr_3$ counterpart. Interestingly, we find that trace amounts of water improve photoactivity. Through experimental and theoretical analyses, this improvement could be attributed to water-induced structural reorganization of MHP, leading to improved crystal quality and decreased effective masses of charge carriers. This work indicates planar heterojunction helps improve the photoactivity and stability of MHP photocatalyst, and our findings provide insights into the effect of water on MHPs.

1. Introduction

Solar energy conversion and utilization by artificial photosynthesis are among the most promising strategies to address current environmental issues and provide an energy source not suffering from fluctuating availability. So far, much effort has been devoted to exploring various photocatalysts, such as inorganic oxides, nitrides, and sulfides [1,2]. carbon-based materials [3] and metal-coordination compounds [4]. However, most reported photocatalysts suffer from a limited light absorption range and rapid charge carrier recombination. Future practical applications require addressing these challenges. Recently, the excellent light absorption properties of metal-halide perovskites (MHPs) have triggered a breakthrough in various solar harvesting applications [5,6]. MHPs have excellent optical and electronic properties such as a high absorption coefficient, low exciton binding energy, and long carrier diffusion length. Furthermore, their structure seems very defect tolerant

allowing various low-cost processing methodologies [7–10]. Recently, MHP photocatalysts successfully generated solar fuels through CO_2 reduction [11] and H_2 evolution [12], and their performance for light-driven organic synthesis [13] and pollutant degradation [14] is equally promising.

Despite the excellent photocatalytic performance, most reported MHP photocatalysts have limited long-term stability due to their moisture sensitivity [15–18]. In the presence of large quantities of water, MHPs tend to decompose relatively quickly into a PbX_2 (X = I, Br, Cl) precipitate, and dissolved ions ($Cs^+/MA^+/FA^+$ cation, and halide anion) [16,17]. In aqueous environments, saturated halo acid solutions can be used to keep the MHP from decomposing [19]. Alternatively, apolar solvents provide a practical photocatalytic environment for MHPs [13, 20–22]. However, the generation of water and polar reaction products during the photocatalytic processes lead to a deterioration of the performance after several hours of operation [13,21]. In short, MHP

---

* Corresponding authors.
** Corresponding author at: Department of Chemistry, KU Leuven, Celestijnenlaan 200F, 3001 Leuven, Belgium.
E-mail addresses: haowei.huang@kuleuven.be (H. Huang), johan.hofkens@kuleuven.be (J. Hofkens), maarten.roeffaers@kuleuven.be (M.B.J. Roeffaers).

photocatalysis research has been facing issues to achieve long-term stability due to the presence or generation of polar molecules such as water. To slow down the deactivation of MHP, a core-shell structure is a straightforward stabilization method [23]. Also, the addition of drying agents such as anhydrous Na_2SO_4, to absorb the produced water in the reaction system, is an effective way of stabilization [22]. Further, planar heterojunction structure using inorganic oxides as protecting layers to cover the MHP has been demonstrated to improve the stability of MHP solar cells or photoelectrodes [24–26]. On the other hand, selective oxidations of alcohols into aldehydes are important reactions in organic industry [27]. Among them, the selective benzyl alcohol (BA) oxidation has attracted much attention since benzaldehyde (BAD) is one of the essential intermediates for fine chemicals, fragrances and flavoring additives [28]. Compared to the hydrolysis of benzal chloride, the selective oxidation of BA into BAD using O_2 as the oxidant is a highly desired sustainable for industrial application.

Here, we show the construction of a stable solar photocatalyst cell ($NiO_x/CsPbBr_3/TiO_2$), with a planar heterojunction structure, where the NiO_x and TiO_2 serve not only as charge carrier transportation layers but also as MHP protecting layers. When applying to selective oxidation of benzyl alcohol under simulated solar light irradiation, this solar photocatalyst cell displays improved photoactivity (a 7-fold enhancement) and stability (23 versus 18 successive cycles before the activity is lower than the first cycle) compared to the pure $CsPbBr_3$, with an average of production rate 16.3 $\mu mol\ cm^{-2}\ h^{-1}$ for over 90 h, or 23 successive cycles of 4 h each. Interestingly, the solar photocatalyst cell displays a significant increase (80.4%) in performance during the first 56 h or 14 operation cycles. Detailed control experiments reveal that this activity enhancement is related to the water molecules generated during the reaction. This *in-situ* generated water improves the crystal symmetry of $CsPbBr_3$, a result confirmed by density functional theory (DFT) calculations. Through a combination of complementary techniques, we show that this water-induced structural reorganization reduces the charge carrier effective mass, thus enhancing the charge carrier separation and transfer.

2. Experimental section

2.1. Materials

Nickel(II) nitrate hexahydrate ($Ni(NO_3)_2 \cdot 6H_2O$), lead(II) bromide ($PbBr_2$), titanium(IV) oxide (TiO_2), benzyl alcohol (BA), 2-phenylethanol, dimethyl sulfoxide (DMSO), 1-phenylethanol, 4-fluorobenzyl alcohol, ethylene glycol, ethylenediamine and ethanol were purchased from Sigma-Aldrich. Cesium bromide (CsBr) and trifluorotoluene were purchased from Alfa Aesar. All chemicals were used without further purification.

2.2. Photocatalyst fabrication

Prior to the fabrication of photocatalysts, ITO coated glasses were cleaned using an ultrasonic cleaner in detergent, Milli-Q water, acetone and isopropanol for 30 min in sequence [29,30]. After that, the cleaned ITO glasses were dried by nitrogen and then immediately illuminated by a UV-ozone machine for 30 min.

$CsPbBr_3$ photocatalysts were deposited onto ITO coated glasses through a low-temperature solution process by spin-coating. In a typical experiment, 74.5 mg CsBr and 128.5 mg $PbBr_2$ were first dissolved in 1 mL anhydrous DMSO to prepare 0.35 M $CsPbBr_3$ precursor solution. Then, the as-prepared solution was spin-coated onto ITO glass at 1000 rpm for 15 s, followed by 3000 rpm for 75 s. The prepared films were kept on a hot plate immediately at 70 °C for 30 min. $NiO_x/CsPbBr_3/TiO_2$ solar cell photocatalysts were fabricated by a three-step solution-processed technology. Specifically, the prepared 1.0 M $Ni(NO_3)_2 \cdot 6H_2O$ ethylene glycol/ethylenediamine solution was dropped onto glass ITO substrate, followed by spin-coating at 4000 rpm for 40 s, and then

annealed in the air environment at 300 °C for 60 min, to form the NiO_x hole extracting layer. Secondly, $CsPbBr_3$ layer was deposited onto NiO_x layer through the same low-temperature solution process by spin-coating as mentioned above. Finally, a pre-prepared TiO_2 precursor solution (50 mg mL^{-1} in ethanol, where the particle size of the TiO_2 is 21 nm, and the TiO_2 power was suspended in the ethanol solution for 1 h *via* ultrasonication without using any ligands) was spin-coated onto $CsPbBr_3$ at 4000 rpm for 40 s, then annealed at 70 °C for 2 min. Pure NiO_x, TiO_2, $NiO_x/CsPbBr_3$ and $CsPbBr_3/TiO_2$ samples were used as reference, and the preparation process was the same as above. All processes were conducted in a glovebox.

2.3. Characterization

Absorption spectra were obtained by ultraviolet-visible spectrophotometer (UV–vis, Lambda-950) and the absorption coefficient (α) of the thin films was calculated using the following expression: $\alpha = 2.303\ A/t$, where A is absorbance and t is the thickness of thin film. X-ray diffractometer (XRD, Cu Kα1 radiation, $\lambda = 1.5406$ Å) was used to obtain the crystallographic properties of the samples. Scanning electron microscopy (SEM) images of samples were taken with a FEI-Q FEG250 system and cross-sectional SEM images were obtained using FEI Helios Nanolab 600i SEM. The steady-state photoluminescence was recorded on an Edinburgh FLS980, from 490 to 580 nm with 5 nm increments and 1 s integration time, under an excitation wavelength of 480 nm. Fluorescence lifetime data was recorded on a home-built confocal FLIM microscope. Emission from a pulsed 480-nm laser diode (LDH-D-C-485, Picoquant, Berlin, Germany) was cleaned up (Chroma ET485/20x, F49–482, AHF Analysentechnik, Tübingen, Germany) and the laser pulsing was set to 1 MHz (PDL 828 Sepia2, Picoquant). X-ray photoelectron spectroscopy (XPS, Al Kα X-ray source, 1486.6 eV) was employed to investigate the detailed effect of water on perovskite with different cycle times, and the C 1s signal was set to a position of 284.6 eV. Electrochemical measurements were made using a standard three-electrode setup. The reference electrode was Ag/AgCl electrode, and a platinum sheet was used as the counter electrode. Connection to the $CsPbBr_3$ working electrode was immersed in the electrolyte solution. The absorption coefficient (α) of NiO_x, $CsPbBr_3$ and TiO_2 thin films in this region was calculated via equation: $\alpha = 2.303\ A/t$, where A is absorbance and t is the thickness of thin film. The calculated α value of NiO_x, $CsPbBr_3$ and TiO_2 is 2.4×10^4, 4.1×10^4 and 2.5×10^4 cm^{-1} at 400 nm, respectively.

2.4. Photocatalytic activity evaluation

The activity of $CsPbBr_3$ and $CsPbBr_3$-based solar cell photocatalysts were evaluated using selective photocatalytic oxidation of benzylic alcohols. The specific operation procedure for the photocatalytic activity measurements is described as follows: trifluorotoluene solution was first being saturated in a sealed bottle with molecular oxygen for 1 h. After that, $CsPbBr_3$ photocatalysts with an illumination area of 1.0×1.2 cm^2 were put into a 20 mL quartz reactor with 2.5 mL saturated trifluorotoluene and 0.5 mmol BA, and the whole reaction system was kept sealing up and under light illumination using a 150 W Xe lamp with AM 1.5 G filter to simulate the solar light spectrum. After irradiation of 4 h, the liquid was analyzed by Shimadzu GC-2010. The conversion of BA, and selectivity of BA/BAD are defined as follows [13]:

Conversion (%) = $C_0 - C_{BA}/C_0 \times 100\%$

Selectivity (%) = $C_{BAD}/(C_0 - C_{BA}) \times 100\%$

where C_0 is the initial concentration of BA; C_{BA} and C_{BAD} are the concentrations of the reaction substrate and corresponding product of the photocatalytic reaction, respectively.

2.5. Interband absorption by excitons using Elliot model

We have applied a semi-empirical relation suggested by Manoogian and Woolley [31] to the experimentally obtained absorption coefficient near the band edge for all materials under study. This model has been obtained from Elliot's theory of Wannier excitons [32] where the contributions of discrete exciton transitions are added to the continuum transitions and are convoluted with a Lorentzian with a broadening of Γ. The expression is given by [33,34]:

$$\alpha(h\nu) = \quad \alpha_0 \sum_n^\infty \left(\frac{1}{n^3}\right)\left(\frac{\Gamma_n}{2}\right)^2 \Big/ \left[\left(\frac{\Gamma_n}{2}\right)^2 + \left(h\nu - E_g + \frac{R_x}{n}\right)^2\right]$$

$$+ \quad \alpha_1\left\{\frac{\pi}{2} + \arctan\!\left[0\right]\left[\left(h\nu - E_g\right) \Big/ \left(\frac{\Gamma_c}{2}\right)\right]\right\}$$

Here α_0 and α_1 represent the absorption peak at the ground state exciton energy and bandgap, respectively. Γ_n is the full width at half maximum of the Lorentzian and Γ_c accounts for the full width of the continuum excitons. R_x is the exciton binding energy and E_g represents the bandgap. n is an integer and referred to as exciton quantum number. Higher values of n can be neglected due to the n^{-3} dependence of the intensity of the excitons peaks. This equation can be used for bulk semiconductors with exciton binding energies much smaller than the bandgap (Wannier excitons) and describe optical transitions to bound and ionized excitonic states. This theory has been applied to model the band edge of halide perovskites as well [35,36]. The extracted bandgaps are summarized in Fig. S3, Fig. S10 and Fig. S11, and Table S1. The high energy side of the curves cannot be well described with this model either due to a non-parabolicity band effect which is not taken into consideration [33] or the presence of other bands that accounts for carrier absorption. Yet, it fits well to the data at the band edges and the obtained bandgaps are in agreement with the other studies [25].

2.6. XRD structural refinement using Le Bail method

We modeled the scattering patterns using the Le Bail method in Fullprof [37], i.e., refining the unit cell (a, b, c), the scattering offset, the profile parameters (U, V, W), and the peak intensities to match the measured diffraction pattern. Thus, this simple model was robust for determining the relative volume change in the unit cell (Fig. 5d), as it was not necessary to know the structural factor and associated structural parameters (i.e., internal tilting), since they are not considered in this type of analysis. All patterns were indexed to an orthorhombic (Pbnm) γ-phase perovskite and a preferential orientation (i.e., perovskite thin film texture; direction and distribution of the grains) was taken into account.

2.7. Density functional theory calculation

The present calculations have been performed with the Vienna ab initio simulation package (VASP) code, based on density functional theory (DFT). The projector-augmented wave method is used to describe the interaction between ion cores and valence electrons. Atomic structures are optimized using the exchange-correlation functional of Perdew, Burke, and Ernzerhof (PBE). A plane-wave cutoff of 450 eV is used in the calculation. A Monkhorst-Pack $6 \times 6 \times 1$ k-point grid is used to sample the Brillouin zone (BZ). All atoms are allowed to be fully relaxed till the atomic Hellmann-Feynman forces are less than 0.01 eV/Å. The convergence criterion of energy in the self-consistency process is set at about 1×10^{-4} eV.

The effective mass ($m*$) is calculated as the following equation:

$$m* = \hbar^2 \left[\frac{\partial^2 \varepsilon(k)}{\partial k^2}\right]^{-1}$$

Where the k is the wave vector along different directions and the $\varepsilon(k)$

represents the eigenvalues of energy band.

3. Results and discussion

3.1. Characterization of the photocatalysts

A series of CsPbBr$_3$ films and CsPbBr$_3$-based planar heterojunction solar photocatalyst cells (NiO$_x$/CsPbBr$_3$/TiO$_2$) deposited on ITO glass substrates were fabricated via simple low-temperature solution-processing starting from different CsPbBr$_3$ precursor solution concentrations (the detailed process is described in Experimental section). The crystal structure of CsPbBr$_3$ films and solar photocatalyst cells was determined by X-ray diffraction (XRD). Fig. 1a shows the XRD patterns of these CsPbBr$_3$ films, the characteristic diffraction peaks of the orthorhombic (Pnma) space group were found and confirmed by structural refinement using the Le Bail method (Fig. S1) [37]. The XRD pattern of solar photocatalyst cell (Fig. 1b) consists of diffraction peaks from NiO$_x$, CsPbBr$_3$ and TiO$_2$, indicating successful synthesis of these three components. The CsPbBr$_3$ films adopt an orthorhombic crystal phase in the constructed solar photocatalyst cells. The surface morphology of CsPbBr$_3$ perovskite films was characterized by SEM. Scanning electron micrographs of CsPbBr$_3$ films with different precursor solution concentrations (0.05–0.45 M) are shown in Figs. S2a-e, in which the surface coverage of CsPbBr$_3$ film improves gradually from 40.7% to 78.5% with increasing precursor solution concentration (Fig. S2f). Besides, cross-sectional SEM images of CsPbBr$_3$ film and solar photocatalyst cell in Fig. 1c and d confirmed this layer-by-layer structure.

Fig. 2a and b represents the UV-Vis absorption spectra of all as-prepared CsPbBr$_3$ films and solar photocatalyst cells possessing strong visible-light absorption. While an excitonic peak is visible around 520 nm, excitons only make up a small fraction of photogenerated species (approx. 1%) with the majority of absorbed photons leading to free charge carriers [7,38]. The bandgap of these CsPbBr$_3$ films, extracted using Elliott's model [32,35,36] (Experimental section), agrees well with the reported 2.3 eV (Fig. S3) [25]. The NiO$_x$/CsPbBr$_3$/TiO$_2$ solar photocatalyst cell processes strong light absorption in the visible range due to the good absorption coefficient of NiO$_x$, CsPbBr$_3$, TiO$_2$ component (2.4 $\times 10^4$, 4.1 $\times 10^4$ and 2.5 $\times 10^4$ cm^{-1} at 400 nm, respectively) (see Experimental section).

Steady-state and time-resolved photoluminescence (PL) measurements were performed to reveal the photophysical processes in these materials. As shown in Fig. 2c, both CsPbBr$_3$ and NiO$_x$/CsPbBr$_3$/TiO$_2$ display an emission peak at around 525 nm, while the PL intensity of NiO$_x$/CsPbBr$_3$/TiO$_2$ was strongly quenched after the deposition of NiO$_x$ and TiO$_2$ as compared to the uncoated CsPbBr$_3$ film, indicative of improved charge separation and reduced radiative recombination [20]. This is further corroborated by time-resolved PL decay measurements, that revealed significant changes in charge dynamics in the NiO$_x$/CsPbBr$_3$/TiO$_2$ solar photocatalyst cell (Fig. 2d). The luminescence decays of the CsPbBr$_3$ film and NiO$_x$/CsPbBr$_3$/TiO$_2$ are analyzed using a sum of two exponential decays, with two distinct decay constants (τ_j) and amplitudes (A_j). The two decay constants τ_1 and τ_2 extracted here are associated with the bound exciton and free exciton recombination, respectively [39–41]. The solar photocatalyst cell NiO$_x$/CsPbBr$_3$/TiO$_2$ showed a longer lifetime than the pure CsPbBr$_3$ film, with τ_1 and τ_2 increasing significantly (see Fig. 2d), hinting to the effective extraction of the photogenerated charge carriers in CsPbBr$_3$ by NiO$_x$ and TiO$_2$ layers (vide infra) [20,24].

3.2. Photocatalytic performance and stability tests

The photocatalytic performance of the CsPbBr$_3$ films and solar photocatalyst cells (1.0 $\times 1.2$ cm^2) was evaluated under simulated solar light (AM 1.5 G) by studying the selective oxidation of benzyl alcohol (BA, 0.5 mmol) in a nonpolar solvent (trifluorotoluene, 2.5 mL) with
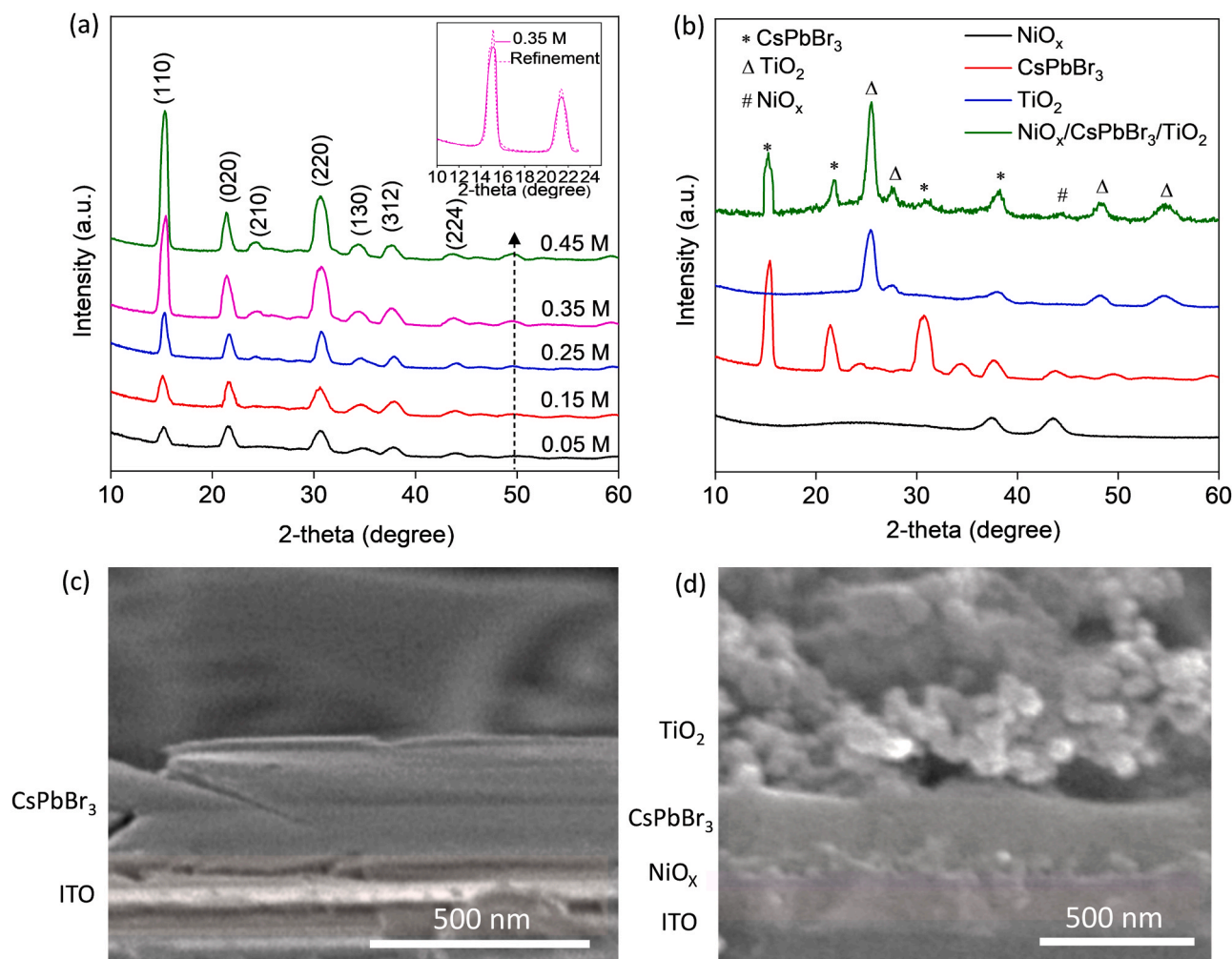
Fig. 1. XRD patterns of (a) CsPbBr$_3$ thin films spin-coated with different precursor concentrations (0.05–0.45 M) and (b) NiO$_x$/CsPbBr$_3$/TiO$_2$ solar photocatalyst cell consists of NiO$_x$, CsPbBr$_3$ and TiO$_2$. (c-d) Cross-sectional SEM of CsPbBr$_3$ thin films and CsPbBr$_3$-based solar photocatalyst cell, respectively.

saturated molecular oxygen under simulated solar light illumination (BA + O$_2$ → BAD + H$_2$O). As shown in Fig. S4, all CsPbBr$_3$ films converted at least 1.1 μmol cm^{-2} h^{-1} BA toward BAD based on the per illumination area [42,43], with an excellent selectivity of over 99%. After the introduction of NiO$_x$ and TiO$_2$, the NiO$_x$/CsPbBr$_3$/TiO$_2$ solar photocatalyst cells presented a significant increase in photoactivity of at least 5.8 μmol cm^{-2} h^{-1} (Fig. 3a) while maintaining over 99% selectivity, in which the optimal photocatalyst cell (NiO$_x$/CsPbBr$_3$/TiO$_2$-4) presented a BAD generation rate of 12.1 μmol cm^{-2} h^{-1} after 4 h of irradiation, a 7-fold enhancement compared to pure CsPbBr$_3$. Gas chromatography–mass spectrometry (GC-MS) was employed to check these products (Fig. S5). In comparison to other reference photocatalysts (Fig. S6a), this planar heterojunction layered system displayed the highest photoactivity. Note that the activity of NiO$_x$/CsPbBr$_3$/TiO$_2$-4 was around 2-fold higher than the sum of the individual components CsPbBr$_3$, NiO$_x$ and TiO$_2$ (Fig. S6b), which can be attributed to the synergistic effect of the charge extraction by NiO$_x$ and TiO$_2$ [20]. Comparison of this solar photocatalyst cell with reported MHP-based catalysts for organic synthesis (Table S2) and selective photocatalytic oxidation BA to BAD over various photocatalysts (Table S3) showed the excellent photocatalytic performance of this solar photocatalyst cell. The production rate of the NiO$_x$/CsPbBr$_3$/TiO$_2$ photocatalyst cell is also comparable to other thin film based photoelectrochemical (PEC) or PEC-photovoltaic (PEC-PV) systems (Table S4). Besides the benzyl alcohol, the efficient conversion of benzylic alcohols, such as 2-phenylethanol, 1-phenylethanol and 4-fluorobenzyl alcohol, confirmed the general applicability of the solar

photocatalyst cell, as summarized in Table S5. Further, to confirm the photocatalytic performance of the proposed photocatalyst cell architecture, we tested the CsPbBr$_3$ films and photocatalyst cells for the selective oxidation of toluene to BAD with saturated molecular oxygen under simulated solar light illumination. The photocatalytic activity is summarized in Fig. S7a, and GC-MS was employed to check the generated products (Figs. S7b-d). Similarly, both CsPbBr$_3$ thin film and photocatalyst cell were effective for photocatalytic oxidation toluene to BAD, with BA as the main side product. Also, the NiO$_x$/CsPbBr$_3$/TiO$_2$ photocatalyst cells presented a significant increase in photoactivity (an 8.7-fold enhancement), compared to the CsPbBr$_3$ counterpart. These results confirmed the versatility of the MHP-based planar heterojunction structure for photocatalytic organic transformation.

The stability of the best solar photocatalyst cell, NiO$_x$/CsPbBr$_3$/TiO$_2$-4, was evaluated by a recycling test in which after 4 h the reaction solution was removed, analyzed and fresh solution was added. As shown in Fig. 3b, the photocatalyst cell showed no activity drops in comparison to the initial one in 23 successive cycles. An average BAD production rate of 16.3 μmol cm^{-2} h^{-1} was achieved for over 90 h of testing. Meanwhile, a selectivity of around 99% was maintained for 23 cycles. The turnover number (TON) is 45300 and turnover frequency (TOF) is 492.4 (h^{-1}) for the first 23 cycles. Furthermore, the recycle test revealed an interesting behavior with an initially improving photocatalytic performance. The highest BAD production rate of 21.7 μmol cm^{-2} h^{-1} was achieved after 14 cycles (56 h in total), a 1.8-fold improvement compared to the initial one (12.1 μmol cm^{-2} h^{-1}). With further reaction cycles, however, the
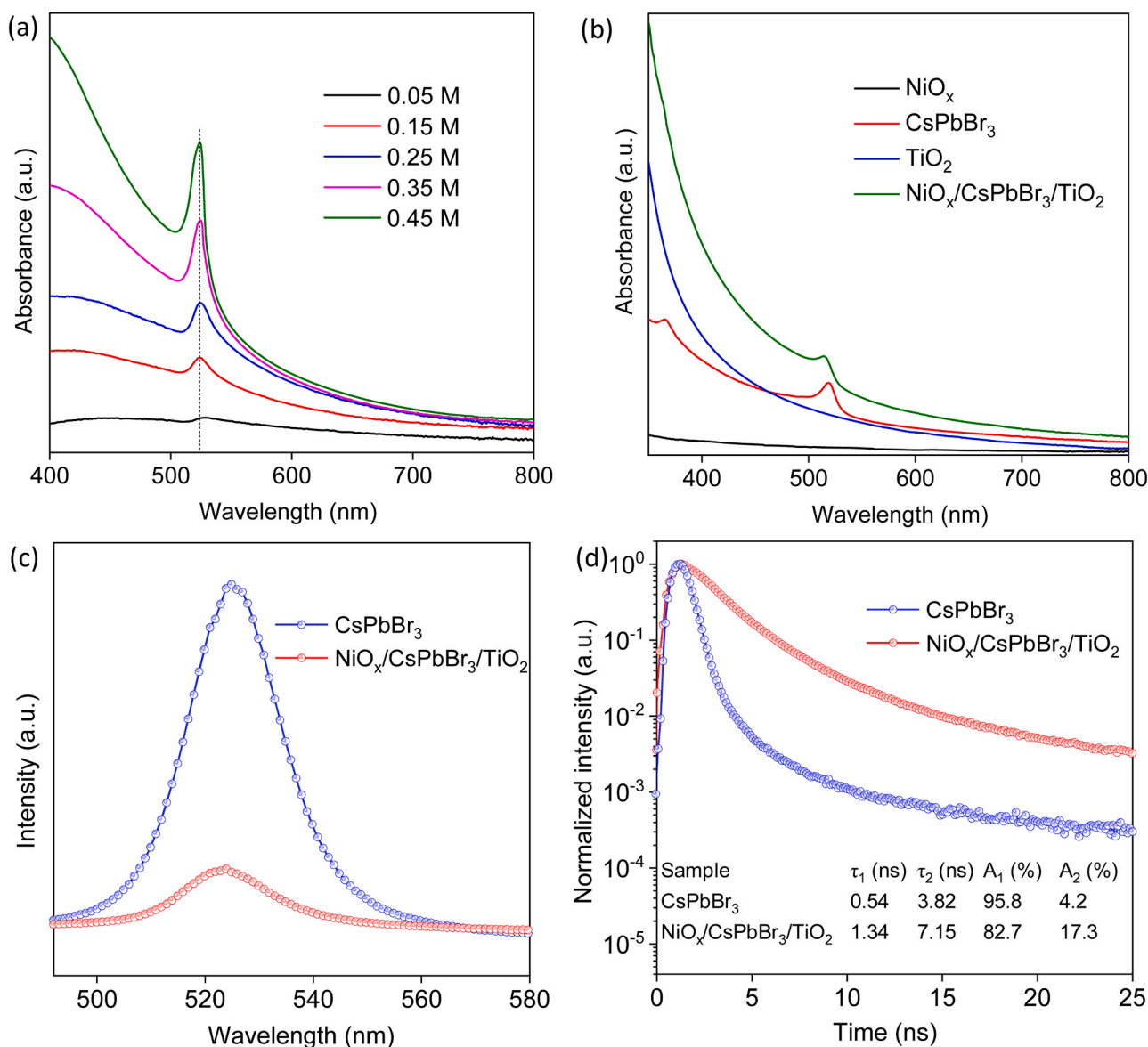
Fig. 2. Absorption spectra of (a) CsPbBr$_3$ thin films with different precursor concentrations and (b) NiO$_x$/CsPbBr$_3$/TiO$_2$ with three components, i.e., NiO$_x$, CsPbBr$_3$ and TiO$_2$. (c) Steady-state PL spectra and (d) PL lifetime decay traces of CsPbBr$_3$ thin film and NiO$_x$/CsPbBr$_3$/TiO$_2$ solar photocatalyst cell.

photocatalytic efficiency gradually decreases. After 23 cycles, the activity of the solar photocatalyst cell is lower than the first cycle testing. The recycle test of the pure CsPbBr$_3$ film photocatalyst also showed a similar tendency as the CsPbBr$_3$-based solar photocatalyst cell, i.e., the photoactivity increases with increasing reaction cycle (Fig. 3b), indicating the CsPbBr$_3$ film itself is the key factor that causes this interesting behavior in photoactivity. The highest production rate of BAD (4.8 μmol cm^{-2} h^{-1}) of CsPbBr$_3$ film photocatalyst was achieved after 11 cycles of 4 h testing (44 h in total). This represents a 3-fold improvement to the first 4 h run, while maintaining a selectivity of around 99%. Note that after the 11th cycle the activity of the CsPbBr$_3$ films is worse than the first cycle. These results indicate that the durability of CsPbBr$_3$ film is inferior to that of solar photocatalyst cell in which NiO$_x$ and TiO$_2$ were deposited on the bottom and top of CsPbBr$_3$, respectively, as the protecting layers. More importantly, to the best of our knowledge, this is the first report on perovskite photocatalysis that the photoactivity increases with reaction time instead of decrease.

3.3. Mechanism study

To elucidate the pathways of photogenerated charge carriers, the energy band structure of the NiO$_x$/CsPbBr$_3$/TiO$_2$ photocatalytic cell was investigated. As shown in Fig. 3c, the valence maximum (VBM) and conduction band minimum (CBM) of CsPbBr$_3$ are -5.6 eV and -3.3 eV, respectively. The VBM of NiO$_x$ is -5.4 eV, and the CBM of TiO$_2$ is -4.0 eV. Therefore, the photogenerated electrons and holes can be easily extracted and transfer to TiO$_2$ and NiO$_x$, respectively [20], to participate in the reaction. Furthermore, to understand the mechanism of photocatalytic selective BA oxidation reaction over the photocatalyst cell, different radical scavengers, i.e., ammonium oxalate, potassium persulfate, 1,4-benzoquinone and t-butanol for holes (h$^+$), electrons (e$^-$), superoxide radicals ($\cdot$O^{2-}), and for hydroxyl radicals ($\cdot$OH$^-$), respectively [20], were employed to examine the role of various redox-active species. Fig. 3c shows the effects of these radical scavengers on the photocatalytic performance, and the detailed parameters are listed in Table S6. Scavenging the holes with ammonium oxalate almost completely stops the reaction, and in the presence of potassium persulfate as electron scavenger also resulted in a sharp drop in the
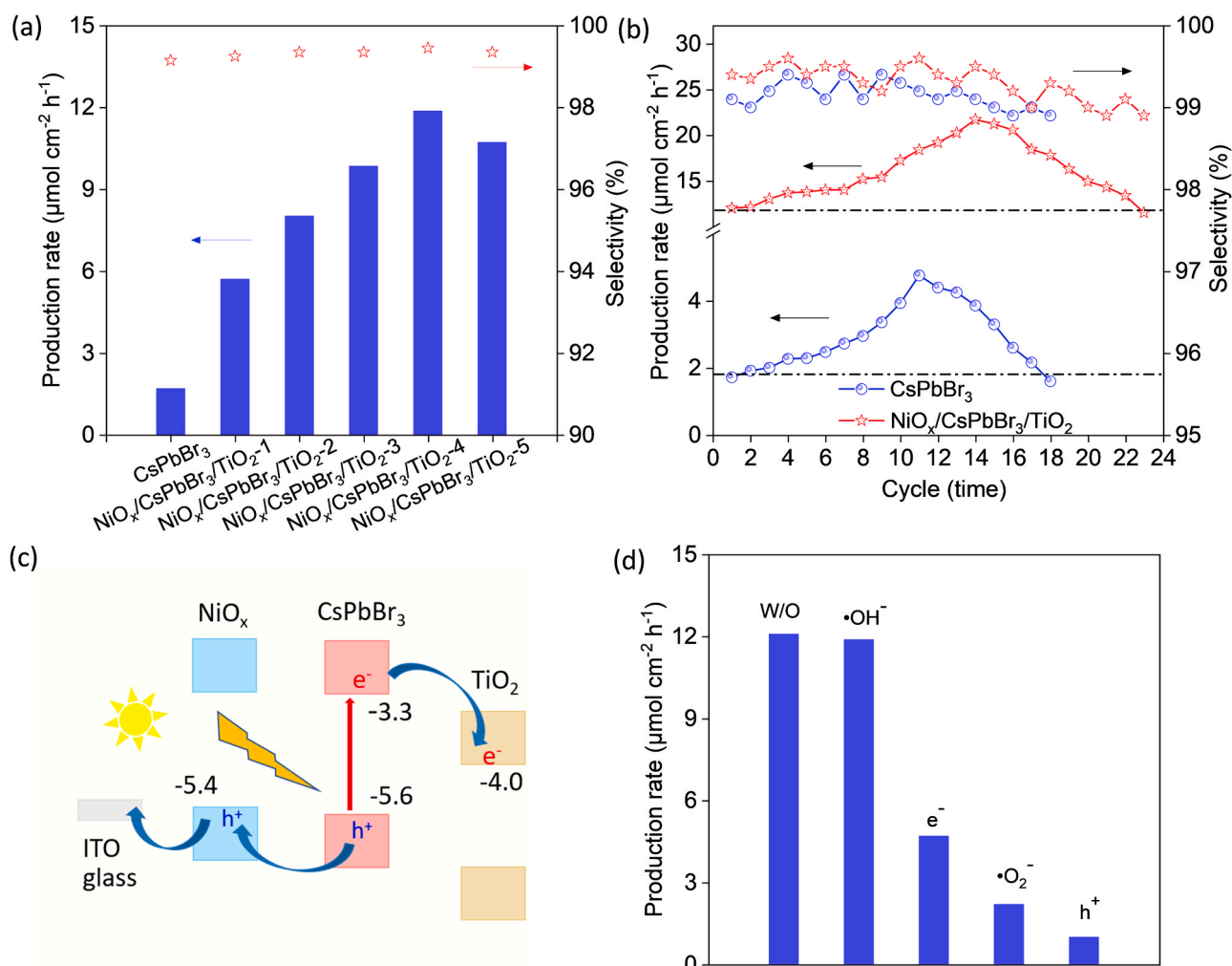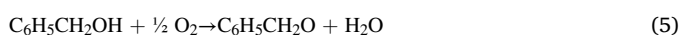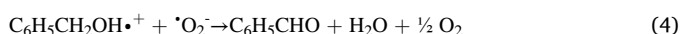
Fig. 3. (a) Selective photocatalytic oxidation of BA to BAD over films of $CsPbBr_3$ and $NiO_x/CsPbBr_3/TiO_2$ photocatalysts, where $NiO_x/CsPbBr_3/TiO_2$-n (n = 1, 2, 3, 4 and 5) represents the precursor solution concentration of $CsPbBr_3$ is 0.05 M, 0.15 M, 0.25 M, 0.35 M and 0.45 M, respectively. (b) Recycling test of $NiO_x/CsPbBr_3/TiO_2$ solar photocatalyst cell and pure $CsPbBr_3$ thin film photocatalyst. (c) The energy band diagram of the photocatalytic cell. (d) The effects of various radical scavengers on the photocatalytic performance of BA oxidation over photocatalyst cell, where W/O represents without scavengers, $\cdot OH^-$, e^-, $\cdot O^{2-}$, and h^+ represents the radical that is targeted by the addition of t-butanol, potassium persulfate, 1,4-benzoquinone and ammonium oxalate additives, respectively. Reaction conditions: photocatalytic cell or $CsPbBr_3$ thin film photocatalysts (1.0 ×1.2 cm^2), 0.5 mmol BA in 2.5 mL trifluorotoluene with saturated molecular oxygen, AM 1.5 G simulated solar light (150 W Xe lamp), reaction time (4 h).

photoactivity; a similar effect is observed when adding 1,4-benzoquinone to the reaction system, while t-butanol has negligible effect on the photoactivity. These results suggest that both holes and electrons actually participate in the BA oxidation reaction. Based on these experiments, we propose following mechanism that responsible for the photocatalytic oxidation of BA over the photocatalyst cell, and the reaction mechanism is as follows [13,21]:

$$CsPbBr_3 + h\nu \rightarrow h^+ + e^- \tag{1}$$

$$O_2 + e^- \rightarrow \cdot O_2^- \tag{2}$$

$$C_6H_5CH_2OH + h^+ \rightarrow C_6H_5CH_2OH\cdot^+ \tag{3}$$

$$C_6H_5CH_2OH\cdot^+ + \cdot O_2^- \rightarrow C_6H_5CHO + H_2O + \tfrac{1}{2} O_2 \tag{4}$$

$$C_6H_5CH_2OH + \tfrac{1}{2} O_2 \rightarrow C_6H_5CH_2O + H_2O \tag{5}$$

Under solar light illumination, $CsPbBr_3$ absorbs solar light to produce electron-hole pairs. Electrons transfer to TiO_2 to reduce the molecular oxygen absorbed on TiO_2 into $\cdot O^{2-}$, species. Meanwhile, the photogenerated holes transfer to NiO_x and oxidize the benzyl alcohol substrates to carbocations. It is well known that dense and uniform thin

films are important for efficient charge separation and transfer in solar cells. While for photocatalysis, besides considering charge separation and transfer, molecules need to directly interact with the photocatalyst to be able to participate in the redox reactions. For the standalone photocatalyst cell-based photocatalysis, different from solar cells, discontinuities in the thin film can serve as the active sites, thus promoting the benzyl alcohol oxidation reaction. Therefore, it is important to establish a balance between the efficient charge separation and sufficient adsorption area. Since both TiO_2 and NiO_x are not fully dense and continuous (Fig. S8), BA substrates and molecular oxygen can be easily adsorbed on non-covered, accessible area and border of NiO_x and TiO_2, respectively. Finally, the BA radical carbocations react with $\cdot O^{2-}$ species to produce the BAD product.

Besides, to reveal the factors that cause the 3-fold improvement in photoactivity over $CsPbBr_3$ films, a series of control experiments were carried out. In these experiments, the role of the solvent (trifluorotoluene), the effect of extended illumination (AM 1.5 G, simulated solar light), and molecular adsorption of BA and BAD were explored (Fig. 4a). Solvent and photodegradation were ruled out, and the presence of BA or BAD only had a minute effect on the activity. Another factor that should be taken into consideration is the generation of water
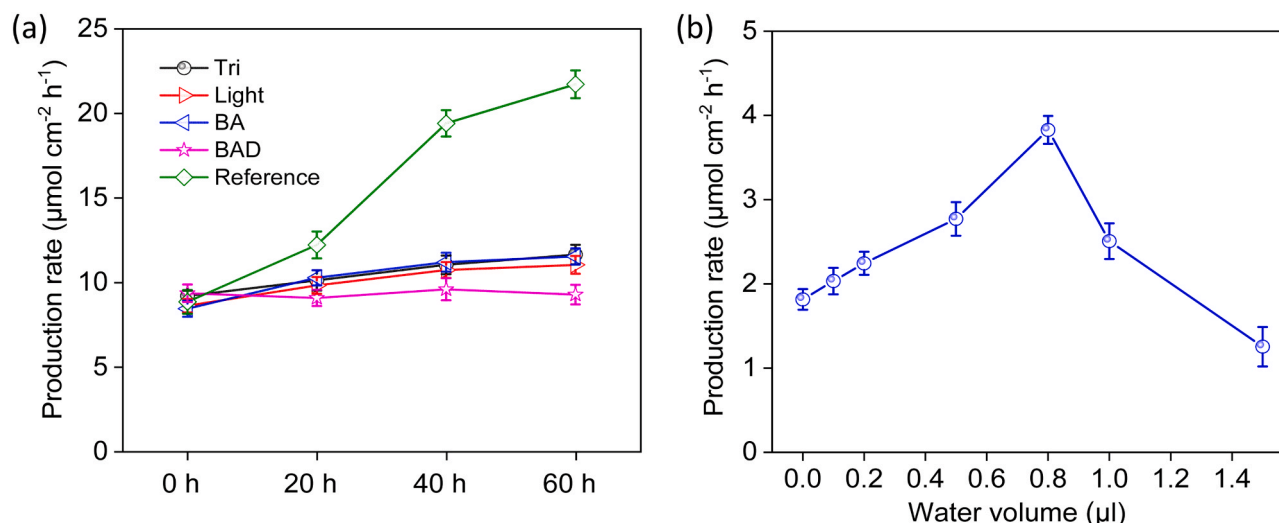
Fig. 4. (a) The effect of solvent (trifluorotoluene), light irradiation (AM 1.5 G, simulated solar light), substrate (benzyl alcohol) and main product (benzaldehyde) on photocatalytic activity for 60 h with an interval of 20 h. (b) Photocatalytic activity (4 h) of CsPbBr$_3$ thin film photocatalyst as a function of the added amount of water to the reaction system. Reaction conditions: CsPbBr$_3$ photocatalyst (1.0 ×1.2 cm^2), 0.5 mmol benzyl alcohol in 2.5 mL trifluorotoluene solution with saturated molecular oxygen, AM 1.5 G simulated solar light irradiation (150 W Xe lamp), illumination time (4 h). With Tri, Light, BA, BAD and Reference referring to storage of the CsPbBr$_3$ thin film before photocatalytic testing in: (1) Tri: 2.5 mL trifluorotoluene in dark. (2) Light: 2.5 mL trifluorotoluene solution under AM 1.5 G simulated solar light illumination. (3) BA: 2.5 mL trifluorotoluene solution with 0.5 mmol benzyl alcohol in dark. (4) BAD: 2.5 mL trifluorotoluene with 0.03 mmol benzaldehyde in dark. While Reference sample is the CsPbBr$_3$ thin film used for the cycling test, with the identical reaction conditions as above.

during the photocatalytic oxidation reaction of BA. To simulate experimental conditions, controlled amounts of water were added to the reaction system while keeping the sample in dark for 4 h, before starting the photocatalytic testing; the water amounts are in the same order of magnitude as those photo-catalytically generated during the process. Fig. 4b shows the significant effect of water on the measured photocatalytic performance. Specifically, the BAD generation steadily improved 2-fold, with 0.8 µL water incubation, before slowly decreasing

again with large amounts of water. These results strongly suggest the beneficial effects of trace amounts of water on the catalytic performance, while excessive water has an adverse effect.

To determine the underlying mechanism of this beneficial effect, changes in the structural properties of CsPbBr$_3$ with increasing cycle times were studied. The XRD patterns in Fig. 5a show similar diffraction peaks for the recycled MHP films. However, changes are visible when analyzing the peak position and peak width in detail, as shown in
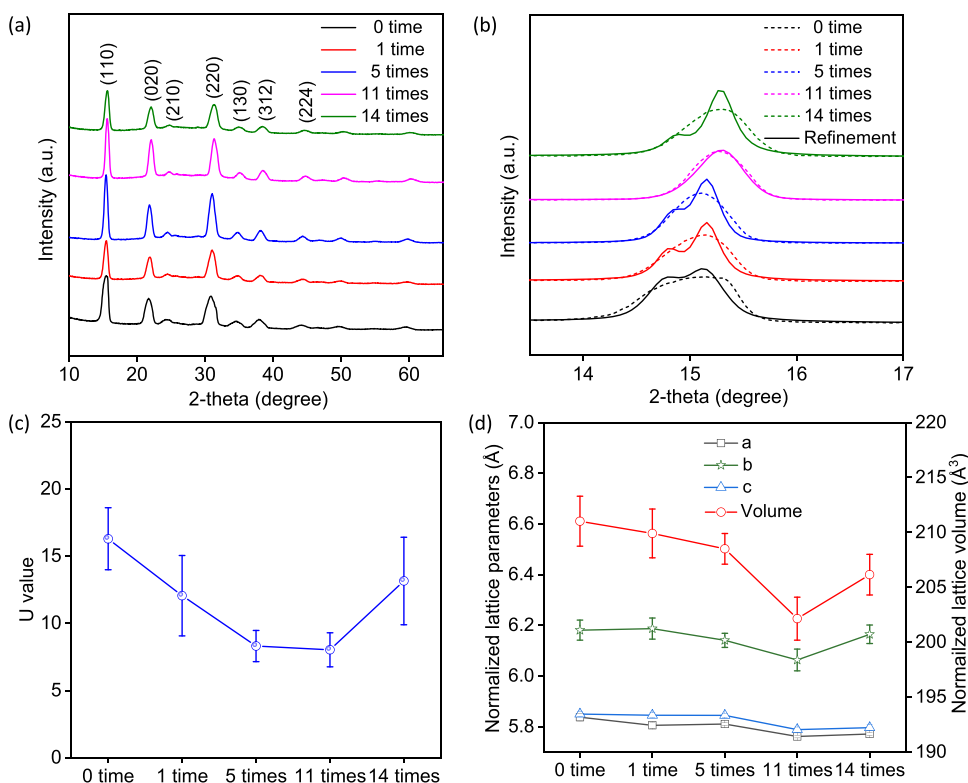

Fig. 5. (a) XRD patterns of CsPbBr$_3$ films recorded before photocatalytic testing, after 1, 5, 11, and 14 testing cycles. (b) Magnified view of XRD patterns of CsPbBr$_3$ films before and after photocatalytic testing on the most prominent diffraction signal recorded around 15 degrees, with the structural refinement via Le Bail method. (c-d) Dependence of the recorded XRD peak broadening and lattice parameters, respectively, on the photocatalytic recycling (derived from the use of a dominant empirical broadening parameter U during the structural refinement (Le Bail method). The other key experimental parameters, like layer thickness and instrumental geometry, are kept constant. Normalization of the γ-phase lattice is made via rescaling the orthorhombic unit cell by (1/√2, 1/√2, 1/2), with the pseudo-cubic unit cell volume also being normalized by the same fractions.

Fig. 5b. Refining the data with the Le Bail method (Fig. S9) [37] reveals the peak-width parameter U (a resolution function parameter used to quantify the peak width) declines substantially from 16.28 (cycle 0) to 8.02 (cycle 11) and then increases to 13.14 after the 14th cycle (Fig. 5c); the normalized lattice parameters, as a function of cycles, are plotted in Fig. 5d. Meanwhile, the normalized, pseudo-cubic unit cell volume (per unit formula, determined from the crystallographic data) reduced about 5% from 211.01 Å^3 to 202.13 Å^3 after cycle 11 and expanded to 206.14 Å^3 with further increased cycling to 14 (Fig. 5d, the detailed parameters are shown in Table S7). This indicates that the crystallinity of $CsPbBr_3$ first improves before decreasing [44–46].

To identify the underlying reason for this improved crystallinity, DFT-based simulations were performed. The model started from a clean $CsPbBr_3$ slab with H_2O adsorbed before relaxation; Vienna ab initio simulation package (VASP) codes (details see Experimental section) [47]. As shown in Fig. 6a and b, the calculated bonding angles of Pb-Br-Pb are 172.8° and 166.9° in $CsPbBr_3$+H_2O and pure $CsPbBr_3$ slab, respectively. The result shows that the $PbBr_6$ octahedrons in $CsPbBr_3$ become more symmetrical after surface adsorption of H_2O molecules, consistent with the experimental XRD data.

In addition, DFT calculations revealed a significant drop in effective mass of the charge carriers in the $CsPbBr_3$+H_2O slab; calculated electron effective mass 0.385 m_0 ($CsPbBr_3$) vs. 0.366 m_0 ($CsPbBr_3$ +H_2O) and the effective hole mass reduces from 0.515 m_0 to 0.489 m_0. This lower effective mass relates to higher mobility and lower recombination probability [48].

3.4. Photophysical properties and electronic structures analyses

The transfer and recombination kinetics of charge carriers were experimentally validated with time-resolved PL measurements. Normalized steady-state PL spectra (Fig. 7a) reveal a blue-shift of the emission maximum from 526 nm to 521 nm (0.023 eV) with increasing reaction cycles. This is in agreement with the absorption data (Fig. S10a). While the absorption slightly decreases, the absorption edge shows a slight blue-shift of about 0.026 eV. With this information at hand, time-resolved PL was used to generate insight into the charge carrier dynamics and experimentally validate the observations from DFT. As shown in Fig. 7b, an increase in PL lifetime is observed with increasing reaction cycles (the detailed parameters are shown in

Table S8). The longest lifetime is obtained after 11 cycles, in which the contribution of τ_1 is reduced from 93.4% (0.58 ns) to 86.6% (1.16 ns). Meanwhile, the contribution of τ_2 is increased from 6.6% to 13.4% for the recycled one, with the τ_2 extended from 3.64 to 6.23 ns. Further increasing cycles beyond 11 times leads to a slightly decreased lifetime but still larger than the pristine one. The suppressed exciton recombination and enhanced carrier lifetime are linked to the separation of electron-hole pairs [49]. This result provides clear evidence for the better effective charge separation after water absorption on the surface of $CsPbBr_3$. The prolonged lifetime enhances the probability of photocatalytic surface reaction over unwanted recombination pathways [50, 51]. These findings show that the beneficial effect of trace amount of water can be linked to optimizing the crystal structure and improving the charge carrier migration to the $CsPbBr_3$ surface.

To evaluate changes in the charge-transfer properties, electrochemical impedance spectroscopy (EIS) was performed. Fig. 7c reveals that with increasing cycles, the semicircle radius in the Nyquist plot becomes smaller, signifying a smaller charge-transfer resistance [51]. The details of these semicircles quantified with an equivalent circuit are summarized in Table S9. The resistance decreases from 259 Ohm (before cycle 1) to 172 Ohm (after cycle 11), indicating an improved electronic conductivity [11]. In addition, the photocurrent responses of $CsPbBr_3$ with different cycle times under solar light irradiation were tested to evaluate photogenerated charge carrier dynamics. As shown in Fig. 7d, the photocurrent of $CsPbBr_3$ under repeated cycles, especially the 11th cycle, increases significantly compared to the original one, suggesting more efficiency in conductivity and charge carriers generation [51].

The energy level transition on $CsPbBr_3$ during the cycling tests was explored by XPS. As shown in Fig. 8a, the XPS spectra of the Cs 3d had no significant change in the spectral shape, while the peaks presented a shift of around 0.5 eV (11 times) to higher binding energy (BE). A similar shift was also found in the spectra of Pb 4f and Br 3d, as shown in Fig. 8b and c. Previous research has revealed that the BE shift can be attributed to water (the water molecules acted as an *n*-dopant), which makes the Fermi level position closer to conduction band minimum (CBM) [52,53]. Thus, the generated trace water would increase electron density and accordingly improve reduction ability.

To further investigate the effect of water on band structure of the $CsPbBr_3$ thin-film with different cycles, electrochemical flat band potential (E_{fb}) measurements (Mott–Schottky curves) were carried out as
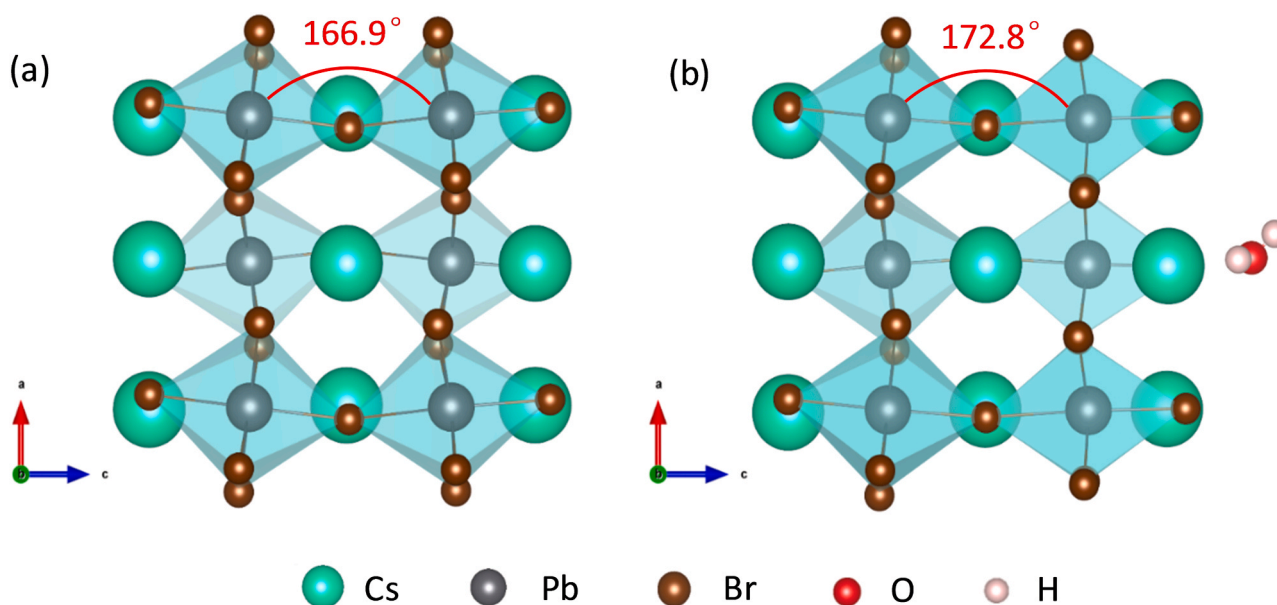

Fig. 6. The models of (a) clean $CsPbBr_3$ slab and (b) $CsPbBr_3$ slab adsorbed H_2O molecules, the calculated bonding angles of Pb-Br-Pb are 166.9° and 172.8° in $CsPbBr_3$ and $CsPbBr_3$+H_2O slab, respectively.
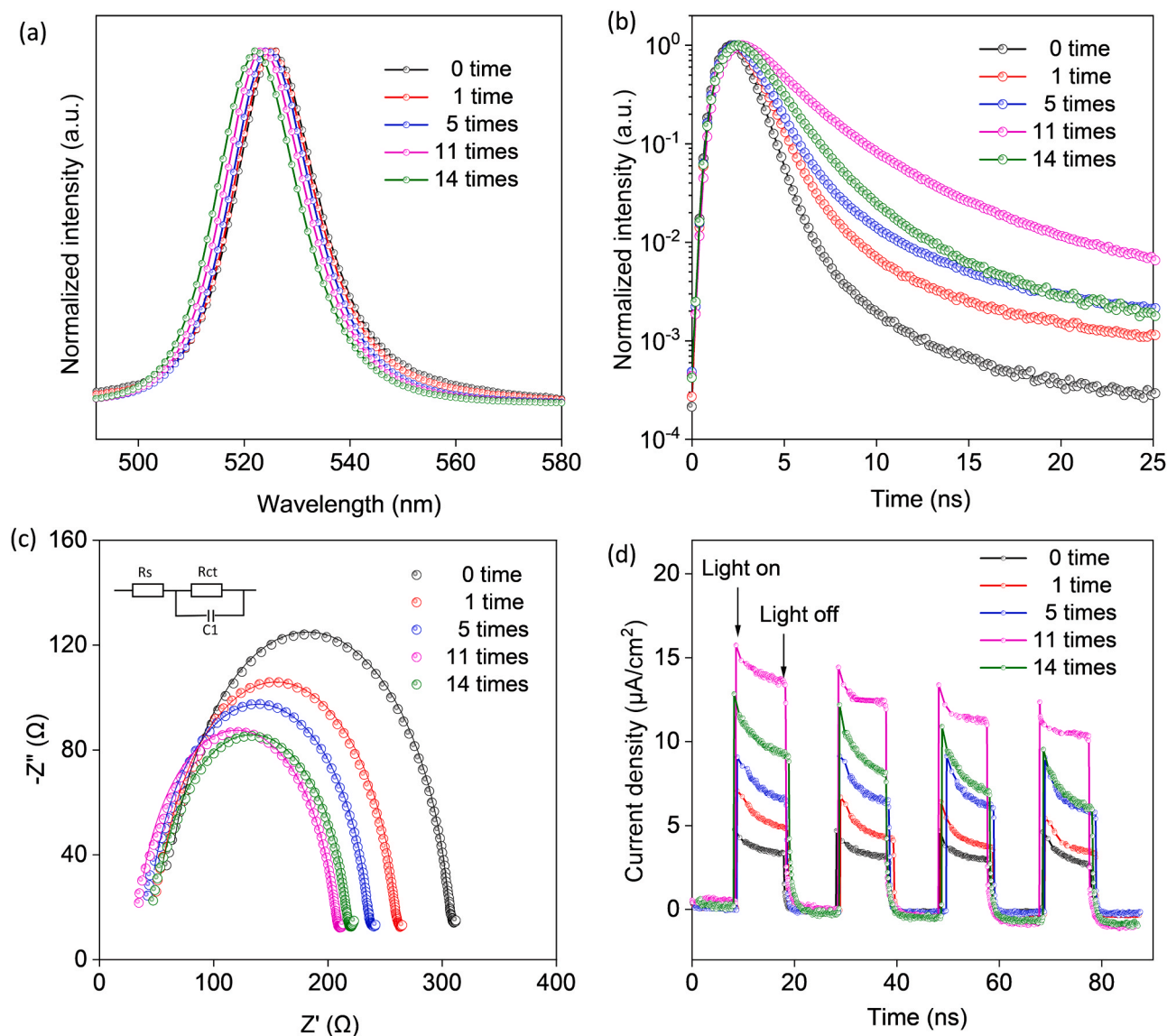
Fig. 7. (a) Steady-state PL spectra, (b) PL lifetime decay traces, (c) Nyquist plots and (d) Photocurrent responses of CsPbBr$_3$ films under repeated reactions with the cycle time of 0 time, 1 time, 5 times, 11 times and 14 times, respectively. The inset in Fig. 7c is the equivalent circuit used to fit the impedance spectra for EIS analysis.

shown in Fig. 8d. The positive slope is characteristic of an *n*-type semiconductor [54]. The calculated E$_{fb}$ of CsPbBr$_3$ with repeated cycles was found to be more negative than that of CsPbBr$_3$ film without photocatalytic use, before cycle 1 E$_{fb}$ = −0.83 V versus Ag/AgCl whereas after cycle 11 it is − 1.07 V. Generally, flat-band potential lies very close to the bottom of the conduction band for *n*-type semiconductors [54,55]. Using the band gap information from the UV–vis spectra (Fig. S10c), the energy band structure of CsPbBr$_3$ is illustrated in Fig. S11. This implies that the conduction band potential becomes more negative with increasing reaction time [54], which responds to the XPS results.

4. Conclusions

In summary, a stable planar photocatalyst cell NiO$_x$/CsPbBr$_3$/TiO$_2$ is developed that yields on average 16.3 μmol cm^{-2} h^{-1} of BAD from the selective oxidation of BA, for over 90 h testing under simulated solar light illumination. A NiO$_x$ and TiO$_2$ hole and electron extracting layer improve the photogenerated charge extraction from the light-absorbing CsPbBr$_3$ layer while simultaneously protecting it from the environment. Our experimental and theoretical results also indicate the trace amounts

of H$_2$O can drastically enhance the photoactivity (a 3-fold improvement) of the as-generated CsPbBr$_3$ by improving the crystal symmetry and decreasing the effective mass of the charge carriers. This work offers an effective strategy for constructing stable metal halide based photocatalysts via simple solution-processing. Besides, our findings provide deeper insights into the effect of water on MHP material and shed light on the beneficial effect of trace amounts of water to improve the photoactivity of perovskite solar catalyst cell.

CRediT authorship contribution statement

Chunhua Wang: Conceptualization, Investigation, Validation, Data curation, Formal analysis, Writing – original draft. **Haowei Huang:** Writing – review & editing, Supervision, Project administration. **Bo Weng:** Resources, Investigation, Visualization. **Davy Verhaeghe:** Resources, Investigation, Visualization. **Masoumeh Keshavarz**: Resources, Investigation, Visualization. **Handong Jin:** Resources, Investigation, Visualization. **Biao Liu:** Software, Formal analysis. **Haipeng Xie:** Resources, Investigation, Visualization. **Yang Ding:** Resources, Investigation, Visualization. **Yujie Gao:** Resources,
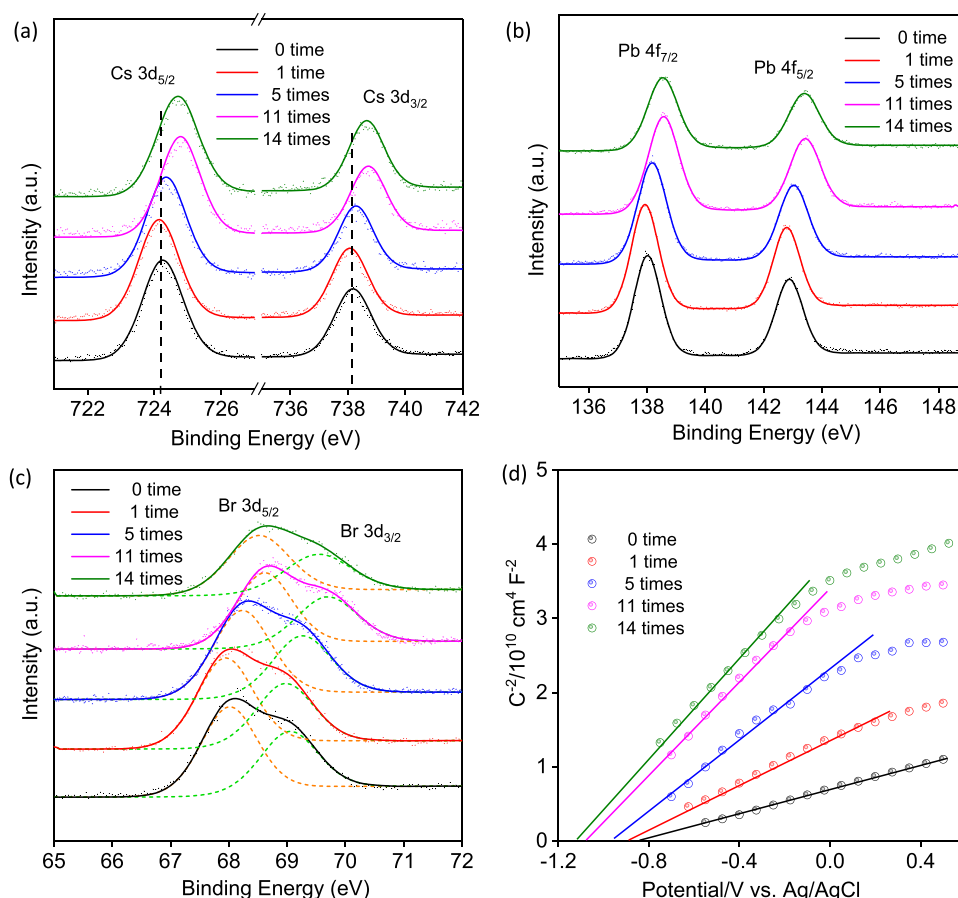
Fig. 8. The XPS spectra of (a) Cs 3d, (b) Pb 4f and (c) Br 3d core levels, and (d) Mott–Schottky plots of CsPbBr₃ films under repeated reactions with the cycle time of 0 time, 1 time, 5 times, 11 times and 14 times, respectively.

Investigation, Visualization. **Haifeng Yuan:** Resources, Investigation, Visualization. **Julian A. Steele:** Resources, Investigation, Visualization. **Johan Hofkens:** Writing – review & editing, Supervision, Project administration. **Maarten B. J. Roeffaers:** Writing – review & editing, Supervision, Project administration.

Declaration of Competing Interest

The authors declare that they have no known competing financial interests or personal relationships that could have appeared to influence the work reported in this paper.

Acknowledgements

Appendix A. Supporting information

Supplementary data associated with this article can be found in the online version at doi:10.1016/j.apcatb.2021.120760.

References

[1] J. Schneider, M. Matsuoka, M. Takeuchi, J. Zhang, Y. Horiuchi, M. Anpo, D. W. Bahnemann, Understanding TiO₂ photocatalysis: mechanisms and materials, Chem. Rev. 114 (2014) 9919–9986, https://doi.org/10.1021/cr5001892.

[2] B. Weng, M.-Y. Qi, C. Han, Z.-R. Tang, Y.-J. Xu, Photocorrosion inhibition of semiconductor-based photocatalysts: basic principle, current development, and future perspective, ACS Catal. 9 (2019) 4642–4687, https://doi.org/10.1021/acscatal.9b00313.

[3] S. Guo, Z. Deng, M. Li, B. Jiang, C. Tian, Q. Pan, H. Fu, Phosphorus-doped carbon nitride tubes with a layered micro-nanostructure for enhanced visible-light photocatalytic hydrogen evolution, Angew. Chem. Int. Ed. Engl. 55 (2016) 1830–1834, https://doi.org/10.1002/anie.201508505.

[4] B. Weng, K.Q. Lu, Z. Tang, H.M. Chen, Y.J. Xu, Stabilizing ultrasmall Au clusters for enhanced photoredox catalysis, Nat. Commun. 9 (2018) 1543, https://doi.org/10.1038/s41467-018-04020-2.

[5] H. Huang, B. Pradhan, J. Hofkens, M.B.J. Roeffaers, J.A. Steele, Solar-driven metal halide perovskite photocatalysis: design, stability, and performance, ACS Energy Lett. 5 (2020) 1107–1123, https://doi.org/10.1021/acsenergylett.0c00058.

[6] M.A. Green, A. Ho-Baillie, H.J. Snaith, The emergence of perovskite solar cells, Nat. Photonics 8 (2014) 506–514, https://doi.org/10.1038/nphoton.2014.134.

[7] D. Luo, W. Yang, Z. Wang, A. Sadhanala, Q. Hu, R. Su, R. Shivanna, G.F. Trindade, J.F. Watts, Z. Xu, Enhanced photovoltage for inverted planar heterojunction perovskite solar cells, Science 360 (2018) 1442–1446, https://doi.org/10.1126/science.aap9282.

[8] C. Wang, C. Zhang, S. Wang, G. Liu, H. Xia, S. Tong, J. He, D. Niu, C. Zhou, K. Ding, Y. Gao, J. Yang, Low-temperature processed, efficient, and highly reproducible cesium-doped triple cation perovskite planar heterojunction solar cells, Sol. RRL 2 (2018), 1700209, https://doi.org/10.1002/solr.201700209.

[9] Q. Jiang, L. Zhang, H. Wang, X. Yang, J. Meng, H. Liu, Z. Yin, J. Wu, X. Zhang, J. You, Enhanced electron extraction using SnO₂ for high-efficiency planar-structure HC(NH₂)₂PbI₃-based perovskite solar cells, Nat. Energy 2 (2016) 1–7, https://doi.org/10.1038/nenergy.2016.177.

[10] H. Zhou, Q. Chen, G. Li, S. Luo, T.-b Song, H.-S. Duan, Z. Hong, J. You, Y. Liu, Y. Yang, Interface engineering of highly efficient perovskite solar cells, Science 345 (2014) 542–546, https://doi.org/10.1126/science.1254050.

[11] G. Gao, Q. Xi, H. Zhou, Y. Zhao, C. Wu, L. Wang, P. Guo, J. Xu, Novel inorganic perovskite quantum dots for photocatalysis, Nanoscale 9 (2017) 12032–12038, https://doi.org/10.1039/c7nr04421f.

[12] Y. Wu, P. Wang, X. Zhu, Q. Zhang, Z. Wang, Y. Liu, G. Zou, Y. Dai, M.H. Whangbo, B. Huang, Composite of $CH_3NH_3PbI_3$ with reduced graphene oxide as a highly efficient and stable visible-light photocatalyst for hydrogen evolution in aqueous HI solution, Adv. Mater. 30 (2018), 1704342, https://doi.org/10.1002/adma.201704342.

[13] H. Huang, H. Yuan, K.P.F. Janssen, G. Solís-Fernández, Y. Wang, C.Y.X. Tan, D. Jonckheere, E. Debroye, J. Long, J. Hendrix, J. Hofkens, J.A. Steele, M.B. J. Roeffaers, Efficient and selective photocatalytic oxidation of benzylic alcohols with hybrid organic–inorganic perovskite materials, ACS Energy Lett. 3 (2018) 755–759, https://doi.org/10.1021/acsenergylett.8b00131.

[14] Z. Zhang, Y. Liang, H. Huang, X. Liu, Q. Li, L. Chen, D. Xu, Stable and highly efficient photocatalysis with lead-free double-perovskite of $Cs_2AgBiBr_6$, Angew. Chem. Int. Ed. Engl. 58 (2019) 7263–7267, https://doi.org/10.1002/anie.201900658.

[15] J. Huang, S. Tan, P.D. Lund, H. Zhou, Impact of H_2O on organic–inorganic hybrid perovskite solar cells, Energy Environ. Sci. 10 (2017) 2284–2311, https://doi.org/10.1039/c7ee01674c.

[16] B. Philippe, B.-W. Park, R. Lindblad, J. Oscarsson, S. Ahmadi, E.M.J. Johansson, H. Rensmo, Chemical and electronic structure characterization of lead halide perovskites and stability behavior under different exposures-a photoelectron spectroscopy investigation, Chem. Mater. 27 (2015) 1720–1731, https://doi.org/10.1021/acs.chemmater.5b00348.

[17] T.A. Berhe, W.-N. Su, C.-H. Chen, C.-J. Pan, J.-H. Cheng, H.-M. Chen, M.-C. Tsai, L.-Y. Chen, A.A. Dubale, B.-J. Hwang, Organometal halide perovskite solar cells: degradation and stability, Energy Environ. Sci. 9 (2016) 323–356, https://doi.org/10.1039/c5ee02733k.

[18] S. Yang, S. Chen, E. Mosconi, Y. Fang, X. Xiao, C. Wang, Y. Zhou, Z. Yu, J. Zhao, Y. Gao, Stabilizing halide perovskite surfaces for solar cell operation with wide-bandgap lead oxysalts, Science 365 (2019) 473–478, https://doi.org/10.1126/science.aax3294.

[19] S. Park, W.J. Chang, C.W. Lee, S. Park, H.-Y. Ahn, K.T. Nam, Photocatalytic hydrogen generation from hydriodic acid using methylammonium lead iodide in dynamic equilibrium with aqueous solution, Nat. Energy 2 (2016) 1–8, https://doi.org/10.1038/nenergy.2016.185.

[20] H. Yuan, H. Yuan, J. Zhao, G. Solis-Fernandez, C. Zhou, J.W. Seo, J. Hendrix, E. Debroye, J.A. Steele, J. Hofkens, C (sp^3)–H Bond activation by perovskite solar photocatalyst cell, ACS Energy Lett. 4 (2018) 203–208, https://doi.org/10.1021/acsenergylett.8b01698.

[21] S. Schünemann, M. van Gastel, H. Tüysüz, A $CsPbBr_3/TiO_2$ composite for visible-light-driven photocatalytic benzyl alcohol oxidation, ChemSusChem 11 (2018) 2057–2061, https://doi.org/10.1002/cssc.201800679.

[22] Y. Dai, C. Poidevin, C. Ochoa-Hernandez, A.A. Auer, H. Tuysuz, A supported bismuth halide perovskite photocatalyst for selective aliphatic and aromatic C-H bond activation, Angew. Chem. Int. Ed. 59 (2020) 5788–5796, https://doi.org/10.1002/anie.201915034.

[23] Z.J. Li, E. Hofman, J. Li, A.H. Davis, C.H. Tung, L.Z. Wu, W. Zheng, Photoelectrochemically active and environmentally stable $CsPbBr_3/TiO_2$ core/shell nanocrystals, Adv. Funct. Mater. 28 (2018), 1704288, https://doi.org/10.1002/adfm.201704288.

[24] J. You, L. Meng, T.-B. Song, T.-F. Guo, Y. Yang, W.-H. Chang, Z. Hong, H. Chen, H. Zhou, Q. Chen, Y. Liu, N. De Marco, Y. Yang, Improved air stability of perovskite solar cells via solution-processed metal oxide transport layers, Nat. Nanotechnol. 11 (2015) 75–81, https://doi.org/10.1038/nnano.2015.230.

[25] J. Liang, C. Wang, Y. Wang, Z. Xu, Z. Lu, Y. Ma, H. Zhu, Y. Hu, C. Xiao, X. Yi, All-inorganic perovskite solar cells, J. Am. Chem. Soc. 138 (2016) 15829–15832, https://doi.org/10.1021/jacs.6b10227.

[26] L.-F. Gao, W.-J. Luo, Y.-F. Yao, Z.-G. Zou, An all-inorganic lead halide perovskite-based photocathode for stable water reduction, Chem. Commun. 54 (2018) 11459–11462, https://doi.org/10.1039/c8cc06952b.

[27] J. Li, M. Li, H. Sun, Z. Ao, S. Wang, S. Liu, Understanding of the oxidation behavior of benzyl alcohol by peroxymonosulfate via carbon nanotubes activation, ACS Catal. 10 (2020) 3516–3525, https://doi.org/10.1021/acscatal.9b05273.

[28] Z. Zhao1, M.M. Flores Espinosa1, J. Zhou, W. Xue, X. Duan, J. Miao, Yu Huang, Synthesis of surface controlled nickel/palladium hydride nanodendrites with high performance in benzyl alcohol oxidation, Nano Res 12 (2019) 1467–1472, https://doi.org/10.1007/s12274-019-2413-9.

[29] J. Huang, C. Wang, Z. Liu, X. Qiu, J. Yang, J. Chang, Simultaneouly enhanced durability and performance by employing dopamine copolymerized PEDOT with high work function and water-proofness for inverted perovskite solar cells, J. Mater. Chem. C 6 (2018) 2311–2318, https://doi.org/10.1039/c7tc05276f.

[30] C. Wang, C. Zhang, S. Tong, H. Xia, L. Wang, H. Xie, Y. Gao, J. Yang, Energy level and thickness control on PEDOT:PSS layer for efficient planar heterojunction perovskite cells, J. Phys. D: Appl. Phys. 51 (2018), 025110, https://doi.org/10.1088/1361-6463/aa9d30.

[31] A. Manoogian, J. Woolley, Temperature dependence of the energy gap in semiconductors, Can. J. Phys. 62 (1984) 285–287, https://doi.org/10.1139/p84-043.

[32] R. Elliott, Intensity of optical absorption by excitons, Phys. Rev. 108 (1957) 1384–1389, https://doi.org/10.1103/physrev.108.1384.

[33] L. Roa, C. Rincon, J. Gonzalez, M. Quintero, Analysis of direct exciton transitions in CuGa ($S_xSe_{1-x})_2$ alloys, J. Phys. Chem. Solids 51 (1990) 551–555, https://doi.org/10.1016/0022-3697(90)90162-9.

[34] G. Marın, C. Rincon, S. Wasim, C. Power, G. Sanchez Perez, Temperature dependence of the fundamental absorption edge in $CuInTe_2$, J. Appl. Phys. 81 (1997) 7580–7583, https://doi.org/10.1063/1.365302.

[35] M. Saba, M. Cadelano, D. Marongiu, F. Chen, V. Sarritzu, N. Sestu, C. Figus, M. Aresti, R. Piras, A.G. Lehmann, Correlated electron–hole plasma in organometal perovskites, Nat. Commun. 5 (2014) 1–10, https://doi.org/10.1038/ncomms6049.

[36] N. Sestu, M. Cadelano, V. Sarritzu, F. Chen, D. Marongiu, R. Piras, M. Mainas, F. Quochi, M. Saba, A. Mura, Absorption F-sum rule for the exciton binding energy in methylammonium lead halide perovskites, J. Phys. Chem. Lett. 6 (2015) 4566–4572, https://doi.org/10.1021/acs.jpclett.5b02099.

[37] D. Balzar, X-ray diffraction line broadening: modeling and applications to high-Tc superconductors, J. Res. Natl. Inst. Stand. Technol. 98 (1993) 321–353, https://doi.org/10.6028/jres.098.026.

[38] D. Marongiu, M. Saba, F. Quochi, A. Mura, G. Bongiovanni, The role of excitons in 3D and 2D lead halide perovskites, J. Mater. Chem. C. 7 (2019) 12006–12018, https://doi.org/10.1039/c9tc04292j.

[39] M. Anni, A. Cretì, Y. Zhang, M.L. De Giorgi, M. Lomascolo, Investigation of the role of the environment on the photoluminescence and the exciton relaxation of $CsPbBr_3$ nanocrystals thin films, Appl. Sci. 10 (2020) 2148, https://doi.org/10.3390/app10062148.

[40] J. Wang, R. Cao, P. Da, Y. Wang, T. Hu, L. Wu, J. Lu, X. Shen, F. Xu, G. Zheng, Purcell effect in an organic-inorganic halide perovskite semiconductor microcavity system, Appl. Phys. Lett. 108 (2016), 022103, https://doi.org/10.1063/1.4939724.

[41] Z. Zhang, Z. Chen, J. Zhang, W. Chen, J. Yang, X. Wen, B. Wang, N. Kobamoto, L. Yuan, J.A. Stride, Significant improvement in the performance of PbSe quantum dot solar cell by introducing a $CsPbBr_3$ perovskite colloidal nanocrystal back layer, Adv. Energy Mater. 7 (2017), 1601773, https://doi.org/10.1002/aenm.201601773.

[42] J. Luo, H. Yang, Z. Liu, F. Li, S. Liu, J. Ma, B. Liu, Organic-inorganic hybrid perovskite-TiO_2 nanorod arrays for efficient and stable photoelectrochemical hydrogen evolution from HI splitting, Mater. Today Chem. 12 (2019) 1–6, https://doi.org/10.1016/j.mtchem.2018.11.001.

[43] S. Lee, G.Y. Jang, J.K. Kim, J.H. Park, Solar-harvesting lead halide perovskite for artificial photosynthesis, J. Energy Chem. 62 (2021) 11–26, https://doi.org/10.1016/j.jechem.2021.02.025.

[44] Z. Li, X. Liu, J. Xu, Y. Liao, H. Zhao, B. Zhang, S.F. Liu, J. Yao, Moisture-induced crystallinity improvement for efficient $CsPbI_{3-x}Br_x$ perovskite solar cells with excess cesium bromide, J. Phys. Chem. Lett. 10 (2019) 4587–4595, https://doi.org/10.1021/acs.jpclett.9b01822.

[45] J.-W. Lee, S.-H. Bae, Y.-T. Hsieh, N. De Marco, M. Wang, P. Sun, Y. Yang, A bifunctional lewis base additive for microscopic homogeneity in perovskite solar cells, Chem 3 (2017) 290–302, https://doi.org/10.1016/j.chempr.2017.05.020.

[46] N. Adhikari, A. Dubey, E.A. Gaml, B. Vaagensmith, K.M. Reza, S.A. Mabrouk, S. Gu, J. Zai, X. Qian, Q. Qiao, Crystallization of a perovskite film for higher performance solar cells by controlling water concentration in methyl ammonium iodide precursor solution, Nanoscale 8 (2016) 2693–2703, https://doi.org/10.1039/c5nr06687e.

[47] B. Liu, M. Long, M. Cai, L. Ding, J. Yang, Interfacial charge behavior modulation in 2D/3D perovskite heterostructure for potential high-performance solar cells, Nano Energy 59 (2019) 715–720, https://doi.org/10.1016/j.nanoen.2019.02.069.

[48] J. Zhang, P. Zhou, J. Liu, J. Yu, New understanding of the difference of photocatalytic activity among anatase, rutile and brookite TiO_2, Phys. Chem. Chem. Phys. 16 (2014) 20382–20386, https://doi.org/10.1039/c4cp02201g.

[49] D. Shi, V. Adinolfi, R. Comin, M. Yuan, E. Alarousu, A. Buin, Y. Chen, S. Hoogland, A. Rothenberger, K. Katsiev, Low trap-state density and long carrier diffusion in organolead trihalide perovskite single crystals, Science 347 (2015) 519–522, https://doi.org/10.1126/science.aaa2725.

[50] P. Niu, L. Zhang, G. Liu, H.-M. Cheng, Graphene-like carbon nitride nanosheets for improved photocatalytic activities, Adv. Funct. Mater. 22 (2012) 4763–4770, https://doi.org/10.1002/adfm.201200922.

[51] J. Oh, J.M. Lee, Y. Yoo, J. Kim, S.-J. Hwang, S. Park, New insight of the photocatalytic behaviors of graphitic carbon nitrides for hydrogen evolution and their associations with grain size, porosity, and photophysical properties, Appl. Catal. B: Environ. 218 (2017) 349–358, https://doi.org/10.1016/j.apcatb.2017.06.067.

[52] Y. Li, X. Xu, C. Wang, C. Wang, F. Xie, J. Yang, Y. Gao, Degradation by exposure of coevaporated $CH_3NH_3PbI_3$ thin films, J. Phys. Chem. C. 119 (2015) 23996–24002, https://doi.org/10.1021/acs.jpcc.5b07676.

[53] C. Wang, Y. Gao, Stability of perovskites at the surface analytic level, J. Phys. Chem. Lett. 9 (2018) 4657–4666, https://doi.org/10.1021/acs.jpclett.8b00381.

[54] X. Xiao, J. Jiang, L. Zhang, Selective oxidation of benzyl alcohol into benzaldehyde over semiconductors under visible light: the case of $Bi_{12}O_{17}Cl_2$ nanobelts, Appl. Catal. B: Environ. 142–143 (2013) 487–493, https://doi.org/10.1016/j.apcatb.2013.05.047.

[55] Y. Su, Z. Han, L. Zhang, W. Wang, M. Duan, X. Li, Y. Zheng, Y. Wang, X. Lei, Surface hydrogen bonds assisted meso-porous WO_3 photocatalysts for high selective oxidation of benzylalcohol to benzylaldehyde, Appl. Catal. B: Environ. 217 (2017) 108–114, https://doi.org/10.1016/j.apcatb.2017.05.075.